



VICTORIA UNIVERSITY
MELBOURNE AUSTRALIA

The effect of ignition protocol on grassfire development

This is the Accepted version of the following publication

Sutherland, Duncan, Sharples, Jason J and Moinuddin, Khalid (2019) The effect of ignition protocol on grassfire development. *International Journal of Wildland Fire*, 29 (1). pp. 70-80. ISSN 1049-8001

The publisher's official version can be found at
<https://www.publish.csiro.au/wf/WF19046>

Note that access to this version may require subscription.

Downloaded from VU Research Repository <https://vuir.vu.edu.au/40493/>

The effect of ignition protocol on grassfire development

D. Sutherland ^{*†‡}; J.J. Sharples ^{†‡}, K.A.M Moinuddin ^{§‡}

September 13, 2019

Abstract

The effect of ignition protocol on the development of grassfires is investigated using physics-based simulation. Simulation allows measurement of the forward rate of spread of a fire as a function of time at high temporal resolution. Two ignition protocols are considered: the inward ignition protocol, where the ignition proceeds in a straight line from the edges of the burnable fire plot to the centre of the plot; and the outwards ignition protocol, where the ignition proceeds from the centre of the burnable fire plot to the edges of the plot. In addition to the two ignition protocols, the wind speed, time taken for the ignition to be completed, and the ignition line length are varied. The rate of spread (R) of the resultant fires is analysed. The outwards ignition protocol leads to a (roughly) monotonic increase in R , whereas the inward ignition protocol can lead to a peak in R before decreasing to the quasi-equilibrium R . The fires simulated here typically take 50 m from the ignition line to develop a quasi-equilibrium R . The results suggest that a faster ignition is preferable to achieve a quasi-equilibrium R in the shortest distance from the ignition line.

*Corresponding author; E duncan.sutherland@adfa.edu.au T +61 2 6268 8884

[†]School of Science, University of New South Wales, Canberra, PO Box 7916, Canberra BC, ACT 2610, Australia

[‡]Bushfire Natural Hazards Cooperative Research Centre, East Melbourne, Victoria, 3002, Australia

[§]Institute for Sustainable Industries and Livable Cities, Victoria University, Melbourne, Victoria, 8001, Australia

17 Introduction

18 Models for rate of fire spread are used extensively in the assessment of wildfire risk. In
19 particular, they are used to assess the likely progression of a fire, which then informs
20 decisions around resource allocation and community safety (e.g. evacuations). Currently,
21 all of the operational rate of spread models used in Australia are empirically based,
22 having drawn upon fire spread data collected through a variety of field-scale experimental
23 programs dating back to the 1950s (Cruz *et al.*, 2015a).

24 Conducting field-scale fire experiments is both labour and cost intensive, involving many
25 months of careful preparation and instrumentation of the experimental plots, conduct-
26 ing the actual experiments, and then analysing the resultant data. As an example, the
27 Annaburroo experiments conducted in the Northern Territory by Cheney *et al.* (1993)
28 involved a total of 170 plots ranging in size from 100 m \times 100 m to 200 m \times 300 m, with
29 121 of them burned and analysed (Cheney *et al.*, 1993). These experiments improved our
30 understanding of the effect of wind speed, dead fuel moisture content and fire line width
31 on rate of spread. Indeed, they underpin the current grassland fire spread model used
32 operationally in Australia. Data from the Annaburroo experiments have also been used
33 to evaluate the performance of physics-based fire spread simulators (Moinuddin *et al.*,
34 2018; Mell *et al.*, 2007).

35 One of the factors that must be considered in fire experiments is the manner in which
36 the fires are initiated. This includes the method used to establish the fire line and the
37 ultimate shape that it assumes – this is an important consideration because it is known
38 that the overall shape of a fire can influence its observed rate of spread (Frangieh *et al.*,
39 2018). The ignition line length also influences the overall shape (Linn and Cunningham,
40 2005) and spread rate Canfield *et al.* (2014) of the fire. In the Annaburroo experiments
41 the fire was ignited by two workers who started at the centre of the upwind edge of the
42 burn plot. The workers then walked slowly in opposite directions with drip torches to
43 ignite the fire. It took approximately one minute to establish the fire line. More recently,
44 Cruz *et al.* (2015b) conducted a number of grassland fire experiments on 33 m \times 33 m

45 plots in Victoria and New South Wales, and adopted a different ignition protocol to that
46 used by Cheney *et al.*. In these experiments, two workers with drip torches started at
47 opposite corners of the upwind edge of the burn plot and quickly moved towards each
48 other, joining the fire line at the centre of the burn plot (Cruz *et al.*, 2015b).

49 The ignition protocol adopted by Cruz *et al.* was chosen so that the experimental fire
50 would develop to a quasi-equilibrium state more quickly (M.Cruz, pers. comm.). On
51 this point, it is important to recognise that the primary aim of operational fire spread
52 prediction systems is to predict the rate of spread of a fire once it has reached a quasi-
53 equilibrium state. Hence, it is desirable that the fire attains this state for as long as
54 possible during the experimental burn. However, regardless of the reason for choosing one
55 ignition protocol over another, it is natural to question how differences in ignition protocol
56 might affect the subsequent development of the fire. This question is particularly pertinent
57 when existing empirical models are refined or updated based on new data obtained from
58 experiments that may have used different ignition protocols to the original experiments.
59 The impact of differing ignition protocols on an updated empirical model is difficult to
60 estimate. If experimental data is taken from any quasi-equilibrium fire, then the data
61 nominally will be consistent. However, the quasi-equilibrium state may be quite difficult
62 to judge, especially from measurements at large time intervals. It is currently unclear
63 how ignition protocol effects the development of the fire to its quasi-equilibrium rate of
64 spread. In physics-based simulations, the fire location data is known at high temporal
65 resolution and therefore it is easy to measure the development of R to quasi-equilibrium
66 values.

67 This study seeks to answer the question: do different ignition protocols significantly affect
68 the quasi-equilibrium rate of spread of the fire and the time taken for the fire to develop to
69 a quasi-equilibrium state? Specifically, physics-based simulations of fires in grassland are
70 used to investigate the differences in R resulting from different ignition protocols, while
71 all other factors are kept the same.

72 Physics-based modelling

73 The physics based model Wild Fire Dynamics Simulator (WFDS 6.0.0, subversion 9977)
74 was used for this study. WFDS solves the governing equations for low-Mach number
75 buoyant flow using a finite difference scheme and radiative heat transfer using a finite
76 volume method. The thermal degradation of vegetative fuel was modelled using a semi-
77 empirical approach where the mass loss rate of the fuel was modelled by a linear equation
78 fitted to data. A mixed-is-burned combustion model (McGrattan *et al.*, 2013) was used
79 so that fuel gasses undergo the combustion reaction, and release heat, when the con-
80 centration of gasses in a computational grid cell exceeds the stoichiometric ratio for the
81 combustion reaction. Turbulent processes are modelled using the principle of Large Eddy
82 Simulation (LES). Large fluid structures are resolved explicitly but smaller sub-grid-scale
83 turbulent processes are modelled. The combustion model and LES are discussed in detail
84 by McGrattan *et al.* (2013) and McDermott *et al.* (2011).

85 The simulations presented here are an extension of Moinuddin *et al.* (2018). As such, the
86 domain size, configuration, and grid resolutions used in the present study are identical to
87 Moinuddin *et al.* (2018). The simulations were performed over a domain that is 960 m
88 long, 640 m wide and 100 m high. The inlet wind velocity was prescribed as a 1/7th-power
89 law model following previous efforts (Moinuddin *et al.*, 2018; Mell *et al.*, 2007; Morvan
90 *et al.*, 2013) and the inlet wind speed U_2 was specified at 2 m above the ground. That is,

$$u_{in}(z) = U_2 \left(\frac{z}{2} \right)^{\frac{1}{7}}. \quad (1)$$

91 Note there is no prescribed synthetic inlet turbulence. The long fetch before the burning
92 domain allows the flow to develop naturally through the domain. There is a sudden
93 change of surface properties, a smooth no-slip boundary transitions to grass modelled
94 with an aerodynamic drag, at 20 m from the inlet. The sudden transition in surface
95 roughness causes the flow to develop turbulence. Coincidentally, the inlet velocity U_2 is
96 approximately the same as u_{10} over the fire ground. For the three inlet velocities the
97 $u_{10} = 2.7, 6.2, 10.7 \text{ m s}^{-1}$. The temperature is constant on all boundaries.

98 The simulation domain was composed of multiple subdomains. Adjacent to the inlet is a
 99 non-burning subdomain of length 660 m. The burnable grass plot, which has dimensions
 100 104 m \times 108 m to mimic the Annaburroo experiments (Cheney *et al.*, 1993), was placed
 101 downwind after the first subdomain. A non-burnable subdomain (approximately 200 m
 102 long) is placed downwind of the burnable plot and upwind of the open outlet boundary.
 103 Bordering subdomains (approximately 270 m wide) are placed on either side of the burn-
 104 able plot. A schematic of the computational domain showing the location of the burn
 plot and the fine grid is shown in Figure 1.

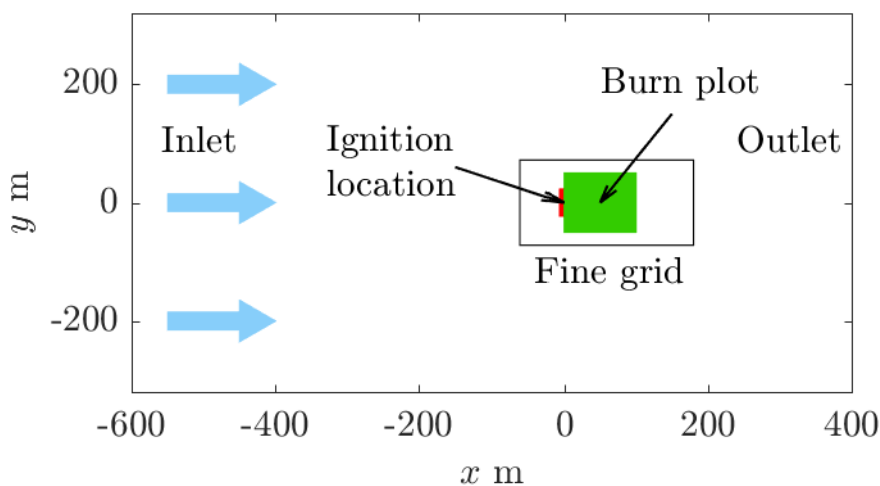


Figure 1: A plan view schematic of the computational domain. The burnable area is shown in green, and the fine 0.25 m \times 0.25 m \times 0.25 m grid is also depicted. The red line marks the location of the line ignitions used in the simulations. The blue arrows represent the applied driving wind.

105

106 Precursor simulations, conducted without burning, were used to ensure the atmospheric
 107 boundary layer above the grassland was well-developed. The flow was considered well-
 108 developed when only turbulent fluctuations were observed in the velocity profile over the
 109 burnable plot. To reduce computational spin-up time, the velocity fields obtained from
 110 the precursor simulations were used to initialise all the fire simulations.

111 Following Moinuddin *et al.* (2018) a grid resolution of 0.25 m in all directions was used
 112 over the burnable grass plot up to a height of 6 m above the grass surface. Coarser
 113 resolutions, again identical to those used by Moinuddin *et al.* (2018) were used in the

114 non-burning subdomains. The fires considered here are of similar size and intensity to
115 the fires studied by Moinuddin *et al.* (2018). It is important to ensure the simulation
116 results are not influenced by the choice of grid resolution or domain size. Moinuddin
117 *et al.* (2018) investigated multiple grid resolutions including stretched grids. Because
118 stretched grids were found to not yield grid independent results we will discuss only
119 uniform grid independence tests. Three grid sizes were considered: coarse 0.5 m resolution,
120 medium 0.25 m resolution, and fine 0.167 m resolution. The frontal location and R_{qe} for
121 the medium and fine resolution simulations were almost identical whereas, the coarse
122 resolution gave a R_{qe} of approximately half the value for the medium and fine resolution
123 grids. Therefore, the 0.25 m resolution was selected for these simulations. Moinuddin
124 *et al.* (2018) also investigated three domain sizes. The domain sizes considered were: the
125 small domain 640 m long \times 440 m wide \times 60 m height, the medium domain 960 m long
126 \times 640 m wide \times 100 m height, and the large domain, 1320 m long \times 760 m wide \times 120
127 m height. The heat release rate, fire front location, and rate of spread for the medium
128 and large domains were found to exhibit only minor differences, whereas the small and
129 medium domain results exhibited differences of nearly 100% in magnitude. Therefore the
130 medium domain was selected.

131 The lateral, top, and downwind boundaries are all open (constant pressure). The ground
132 was a no-slip boundary imposed by a log-law of the wall. The fuel was modelled as a
133 thin layer on the bottom boundary, under the assumption that for large fires most of
134 heat released occurs above the fuel bed and so heat transfer within the fuel bed itself was
135 predominantly in the vertical direction. A separate high-resolution grid was used within
136 the fuel bed to resolve the vertical radiant heat transfer. The drag force of the grassland
137 was modelled using a standard aerodynamic drag force term, using drag coefficient and
138 leaf area index parameters the same as those used by Mell *et al.* (2007).

139 Following Morvan and Dupuy (2004) a linear model of thermal degradation of fuel was
140 used in these simulations. The mass-loss-rate of the solid fuel degrading under heating is
141 assumed to be linear and begins at a critical temperature of 400 K. The degradation of
142 fuel terminates at 500 K. All the thermo-physical, pyrolysis and combustion parameters

143 are identical to those used by Moinuddin *et al.* (2018) and were again selected to replicate
144 the grassfire experiments of Cheney *et al.* (1993). Parameters such as vegetation height
145 (0.21 m) and load (0.283 kg m⁻²) were taken from Mell *et al.* (2007) whereas fuel and
146 thermo-physical parameters; i.e. heat of combustion (16400 kJ kg⁻¹), heat of pyrolysis
147 (200 kJ kg⁻¹), the vegetation char fraction is 0.17, and the soot yield (0.008 unitless), were
148 chosen to match experimental measurements of cellulosic fuel. The vegetation moisture
149 content was 0.063, the surface-to-volume ratio of vegetation was 9770 m⁻¹, the vegetation
150 element density is 440 kg m⁻³, and the drag coefficient is 0.125. The emissivity is 0.99 and
151 the maximum mass loss rate is 0.15 kg s⁻¹ m⁻³. The ambient temperature is 305 K and
152 relative humidity 40%. For further details on the selection of thermophysical, pyrolysis,
153 and combustion parameters see Moinuddin *et al.* (2018).

154 **Varying ignition protocol**

155 The simulated grassfires were ignited along the upwind edge of the burn plot by applying
156 a prescribed heat release rate (HRR) per unit area of 750 kW m⁻² for a duration of
157 4 seconds. The ignition line had a constant width of 2 m, a total length of L_i , and is
158 discretised into eight sections (except for the largest L_i cases where 16 sections were used)
159 of equal length ℓ . To emulate the movement of the ignition crews in the experiments of
160 Cheney *et al.* (1993) and Cruz *et al.* (2015b), different sections were ignited at different
161 times. In particular, two different models of the ignition process were considered: an
162 inward ignition protocol and an outward ignition protocol.

163 For the inward ignition protocol, the outermost sections of the upwind edge were ignited
164 first. The next innermost sections were then ignited successively in time steps of $\delta t_i =$
165 ℓ/u_i , where u_i is the ignition speed - faster ignition speeds correspond to faster moving
166 workers with drip torches. The outward ignition protocol was modelled in a similar
167 manner, but with the innermost sections ignited first and the next outermost sections
168 successively ignited in time steps of δt_i . In this study three ignition speeds were considered:
169 $u_i = 0.5, 1.0$ and 2.4 m s⁻¹, for each of ignition protocols.

170 To demonstrate the differences in the ignition protocols, fire line contours (for the $U_2 = 6$
171 m s^{-1} , $u_i = 1.0 \text{ m s}^{-1}$ and $L_i = 48 \text{ m}$ case) during the ignition process are shown in
172 Figure 2.

173 The isochrones of the simulated fires were obtained by examining the bottom boundary
174 temperature. Under the linear thermal degradation model used in WFDS, pyrolysis of
175 the solid fuel occurs when the temperature T of the solid fuel, i.e. the bottom boundary,
176 exceeds 400 K. Due to the nature of the ignition protocols, it takes some time before a
177 single continuous fire line is established. As a consequence, the time of ignition is slightly
178 difficult to interpret. In Figure 2, time is measured from when ignition commences,
179 either at the outer edges for the inward protocol, or at the centre of the plot for the
180 outward protocol. Initially, the inward ignition fire (Fig. 2b) lags slightly behind the
181 outward ignition fire (Fig. 2a), but ultimately overtakes it. Over the entire simulation
182 period shown in Figure 2, the inward ignition fire spreads about 12% further than the
183 outward ignition fire. To clarify the three-dimensional shapes of the two fires (U6u1L48i
184 and U6u1L48o), two renderings of the flame and soot mass fraction are shown in Figure
185 3. These images were made using the WFDS companion program Smokeview (Forney,
186 2019). The flame was visualised using the 80 kW m^{-3} isosurface of heat release rate per
187 unit volume. The fires are both shown at 21 s after the ignition process commences. The
188 smoke plume of the inward ignition fire is more vertical than the smoke plume of the
189 outward ignition fire, suggesting that the inward ignition fire is more intense at that point
190 in time.

191 **Parameter space**

192 All simulations were performed with both the inward and outward protocols. The effect of
193 ignition line speed u_i , inlet wind speed U_2 , and ignition line length L_i were all investigated
194 independently.

195 Inlet wind speeds of $U_2 = 3, 6, 10 \text{ m s}^{-1}$ were considered. The varying wind speed simu-
196 lations were performed with $u_i = 1.0 \text{ m s}^{-1}$ and $L_i = 48 \text{ m}$.

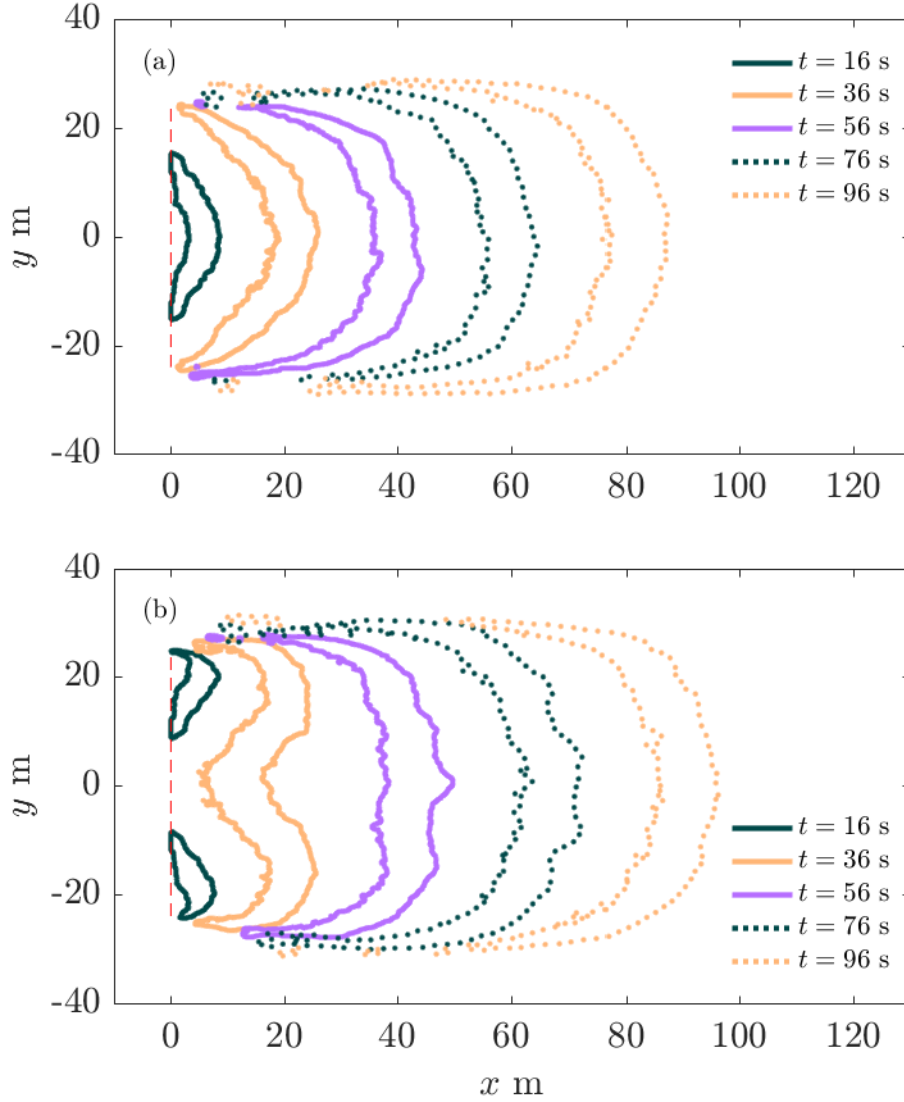


Figure 2: The simulated isochrones of the fire at the times shown; contours of the boundary temperature at $T = 400$ K for (a) the case U6u1L48o, that is outward ignition, and (b) U6u1L48i, inward ignition.

197 Finally, four ignition line lengths were considered: $L_i = 12, 24, 48, 96$ m. In these simula-
 198 tions the wind speed and ignition speed were held constant at $U_2 = 6$ m s $^{-1}$ and $u_i = 1.0$
 199 m s $^{-1}$, respectively. The largest ignition line length was chosen to better reflect the rec-
 200 ommendations of Cheney and Gould (1995) who suggest that an ignition line length of
 201 100 m or more is required for a fire to reach a quasi-equilibrium rate of spread. The
 202 $L_i = 48$ m matches the simulations of Moinuddin *et al.* (2018); Mell *et al.* (2007). The
 203 smaller ignition lengths were chosen to be commensurate with more modern experimental
 204 protocols; for example, Cruz *et al.* (2015b).

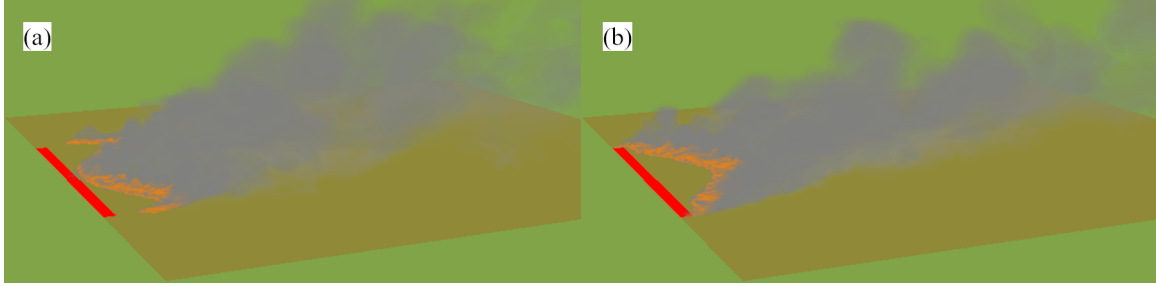


Figure 3: The fire fronts at 21 s after the ignition process commences rendered using Smokeview (Forney, 2019). The flame is visualised with the 80 kW m^{-3} isosurface of heat release rate per unit volume and the smoke is visualised with the soot mass fraction. (a) U6u1L48i (b) U6u1L48o.

205 An infinite speed ignition, that is instantaneous ignition along the entire length of the
 206 upwind edge, was also simulated as a control. The infinite ignition speed simulation was
 207 conducted with the wind speed and ignition line length held constant at $U_2 = 6 \text{ m s}^{-1}$
 208 and $L_i = 48 \text{ m}$ respectively.

209 The defining parameters for each experiment are listed in Table 1. Note that in the
 210 simulation names the first number denotes the driving wind speed, the second number
 211 the ignition speed, and the third number the ignition line length. The ‘i’ or ‘o’ at the
 212 end of the simulation name denotes whether the ignition protocol is inward or outward,
 213 respectively. For example, ‘U3u1L48o’ denotes the simulation where the driving wind
 214 speed is 3 m s^{-1} , the ignition speed is 1.0 m s^{-1} , the ignition line length is 48 m , and
 215 the ignition protocol is outwards. It is of interest to note that ‘U6u1L48o’ matches case
 216 C064 from the Annaburroo experiments (Cheney *et al.*, 1993), which has been considered
 217 previously by Moinuddin *et al.* (2018) and Mell *et al.* (2007). The U6u1L48o case is
 218 identical to the 6 m s^{-1} , vegetation height 0.21 m of Moinuddin *et al.* (2018). The
 219 U6u1L48o case, is similar but not identical to the C064 case studied by Mell *et al.* (2007).
 220 The values of soot yield, the vegetation char fraction, vegetation element density, and
 221 vegetation heat of pyrolysis used here were also different to the values used by Mell *et al.*
 222 (2007). Mell *et al.* (2007) observed more spread on the lateral edges of the fire, than was
 223 observed by Moinuddin *et al.* (2018). Moinuddin *et al.* (2018) obtained results which were
 224 in better agreement with the experimental data of Cheney *et al.* (1993). The simulations
 225 of Mell *et al.* (2007) were conducted with 1 m resolution, compared to 0.25 m resolution

226 used here. The finer grid resolution is likely the reason for the slower lateral spread of
 227 the fire.

Simulation	U_2 (m s ⁻¹)	u_i (m s ⁻¹)	L_i (m)
U3u1L48i, U3u1L48o	3	1.0	48
U6u1L48i, U6u1L48o	6	1.0	48
U6uInfL48	6	∞	48
U10u1L48i, U10u1L48o	10	1.0	48
U6u0.5L48i, U6u0.5L48o	6	0.5	48
U6u2.4L48i, U6u2.4L48o	6	2.4	48
U6u1L12i, U6u1L12o	6	1.0	12
U6u1L24i, U6u1L24o	6	1.0	24
U6u1L96i, U6u1L96o	6	1.0	96

Table 1: Simulation cases and defining parameter values.

228 Wind field development and its effect on fire spread

229 The simulated driving wind field should seek to replicate an atmospheric surface layer
 230 as closely as practicable and it is desirable that turbulent fluctuations in the simulations
 231 are statistically stationary. Experimental fires may experience strong gusts, i.e. large
 232 departures from the mean velocity that persist for significant times, leading to changes
 233 in the rate of spread, or the direction of the fire. In these simulations the mean profile is
 234 determined by the imposed inlet profile, equation (1), which is held constant in time. The
 235 flow is allowed to develop naturally through the domain. Because the inlet and initial
 236 conditions are kept constant for the inward and corresponding outward ignition protocol
 237 simulations, the wind field is largely controlled in these simulations. Moinuddin *et al.*
 238 (2018) demonstrate that after approximately $\tau = 4$ domain turnover times ($\tau = L_D/U_2$)
 239 that the flow develops to a log-law profile over the burnable area. The profile that develops
 240 over the simulated grassland is not the same as a log-law over a rough surface. The grass
 241 is modelled as a region of aerodynamic drag, so there is a shear-layer present above the
 242 grassland similar to the shear-layer above a tree canopy (Belcher *et al.*, 2012). Following
 243 Bou-Zeid *et al.* (2004) we fitted a log-law of the form

$$u(z) = \frac{u_*}{\kappa} \log\left(\frac{z}{z_0}\right), \quad (2)$$

244 where $\kappa = 0.4$ is von Karman’s constant, u_* is the friction velocity, and z_0 is the equivalent
245 roughness length. The equivalent roughness length characterises the canopy shear layer as
246 a shift in the log region of the mean velocity profile. Because z_0 captures a shear layer, the
247 measured value of z_0 will therefore be a function of the grass land properties (height, drag
248 coefficient, leaf-area density) and z_0 will also depend on the driving velocity. Figure 4(a)
249 shows the measured profiles and logarithmic fit for the three driving velocities ($U_2 = 3, 6,$
250 and 10 m s^{-1}).

251 Moinuddin *et al.* (2018) compare the time series of u -velocity at $x = 405 \text{ m}$, $y = \pm 50 \text{ m}$,
252 $z = 2 \text{ m}$ (the upstream corners of the burnable plot) to anemometer measurements from
253 the Annaburoo grassfire experiments Cheney *et al.* (1993). The simulated time series of
254 velocity matches the mean of that reported by Cheney *et al.* (1993), however, larger gusts
255 are recorded in the experimental data. While the mean values match the experimental
256 observations, the mean u -velocity at $x = 405 \text{ m}$, $y = \pm 50 \text{ m}$, $z = 2 \text{ m}$ is lower than the
257 prescribed inlet velocity. The time series of the u -velocity at $x = 405 \text{ m}$, $y = \pm 50 \text{ m}$,
258 $z = 2 \text{ m}$ for $U_2 = 3, 6$ and 10 m s^{-1} are shown in Figure 4(b). The $u(405, 50, 2, t)$ for all
259 cases fluctuate around their mean values and therefore the wind fields are well developed.

260 To confirm that the turbulent fluctuations do not significantly effect the smoothed R
261 results (details of the measurement and smoothing of R follow in the next section) a
262 repeated simulation was performed where the ignition was delayed. Note that if the
263 simulation is re-run without alteration, the same results will occur because the fire is
264 subjected to exactly the same atmospheric flow; the initial wind conditions require some
265 perturbation. By delaying the ignition time the fire will experience different turbulent
266 fluctuations. However, because the turbulent fluctuations are statistically stationary, the
267 $R(t)$ of the two simulations should be largely unaffected except for different fluctuations
268 in R . The ignition was delayed by 100 s , which is comparable to the domain turnover
269 time ($\tau = L_D/U_2 = 960/6 = 160 \text{ s}$) for the simulation. The $R(t)$ for the two cases is
270 shown in Figure 4(c). The difference in R is minor, and within the error bars estimated
271 from the smoothing of the R data, which represent an uncertainty of approximately 10%;
272 it is sufficient to use only a single simulation to obtain reliable results with a quantifiable

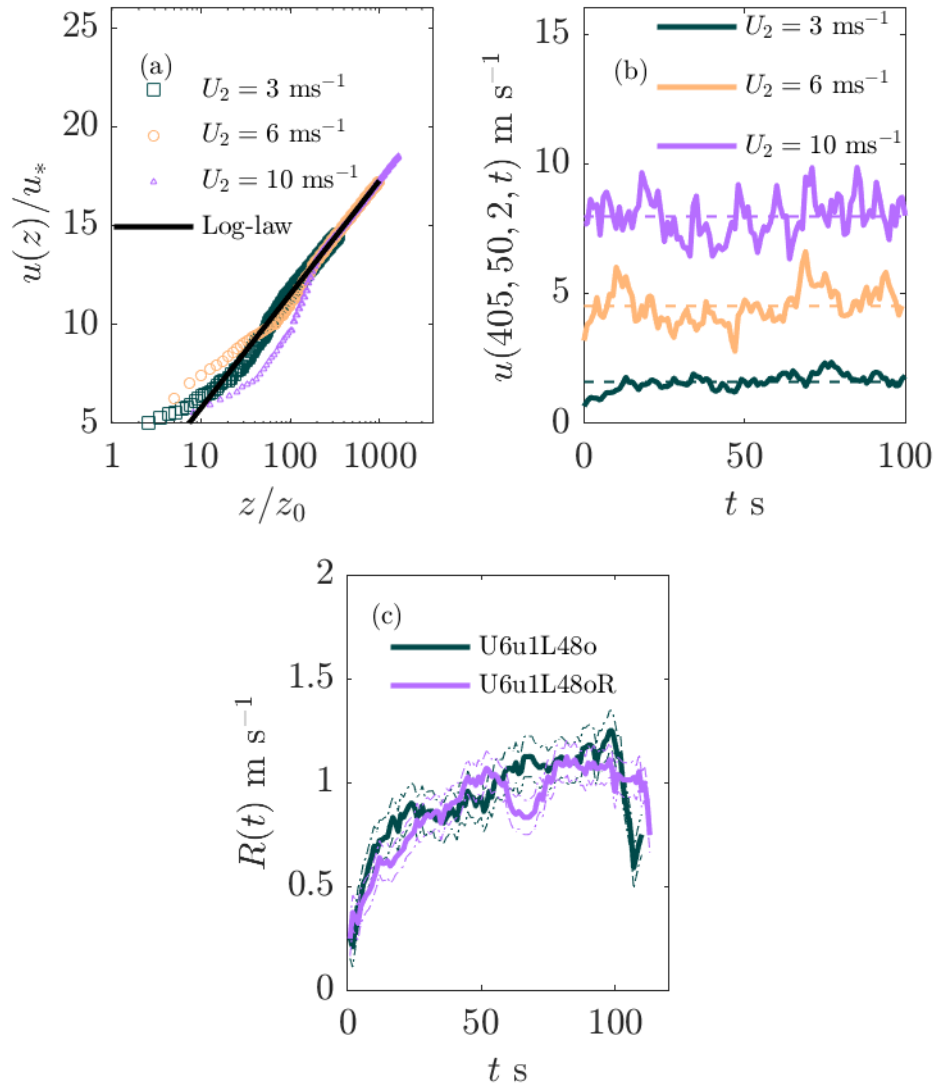


Figure 4: (a) velocity profiles over the fire plot for $u_2 = 3, 6,$ and 10 ms^{-1} and the fitted log-law profile. (b) Time series of $u(405, 50, 2)$ for $u_2 = 3, 6,$ and 10 ms^{-1} , the dashed lines are the time average of the velocity time series. (c) Variation in R for two runs of U6u1L48o

274 Centreline rate of spread development

275 Because the fire is symmetric it is sensible to examine only the geometric centreline of the
 276 fire. At each simulation output time (every 0.5 s) the temperature was extracted along
 277 the centreline of the fire. The head fire was associated with the largest peak in boundary

278 temperature. The fire centre location was identified as $x_*(t) = ((x_1 - x_0))/2 + x_0$, where
279 x_0 and x_1 are the left and right x -locations of where the peak exceeds $T = 400$ K. This
280 definition is analogous to that used by Apte *et al.* (1991).

281 The standard first-order forward finite difference was used to obtain the approximate $R(t)$
282 over time. The $R(t)$ data were smoothed using a 10 point moving average to reduce noise
283 caused by turbulent fluctuations. The variance between the smoothed and raw data was
284 used as measure of uncertainty in $R(t)$. Plotting R as a function of x_* allows assessment
285 of variation in the initial location of the head fire and allows the minimum size of a burn
286 plot required to allow development of a quasi-equilibrium state to be quickly identified.

287 An alternative means of obtaining an averaged, quasi-equilibrium rate of spread, R_{qe} , is
288 to use least-squares regression to fit a straight line to the fire centre location $x_*(t)$ over the
289 region where the fire spread appears linear. The average R_{qe} is then the slope of the fitted
290 line. The region where the fire front is advancing at a constant rate can be subjective
291 to identify. We simply picked the largest time interval where the $R(t)$ appeared to be
292 constant; choosing other slightly different time intervals made very little difference to the
293 R_{qe} . The goodness of fit statistic r^2 between a straight line with slope R_{qe} and the fire
294 front location $x_*(t)$ was always above 0.9.

295 Firstly, we examined R for fixed ignition line length, ignition speed, and wind speed;
296 the only variation is the direction of the ignition line. The R values for U6u1L48i and
297 U6u1L48o are plotted in Figure 5. In this figure, R is plotted against time in panel (a),
298 and against fire distance along the plot in panel (b). Because the inward ignition protocol
299 takes approximately 30 s before a centreline fire is established, R is apparently shifted
300 forward for the U6u1L48i case in figure 5(a). The reason for the lag in centreline R is clear
301 from Figure 2, the fire exhibited a pronounced v-shape as a result of the ignition protocol.
302 The fire front then surged forward leading to the inward ignition fire propagating faster
303 than the outward ignition fire. Rate of spread values $R(t)$ are shown as thick solid lines,
304 while the uncertainties in the simulation results are depicted using thin dashed lines of
305 the same colour. The uncertainties were taken as the smoothed rate-of-spread time series
306 plus or minus the variance of the non-smooth rate-of-spread time series. The uncertainties

307 in R are about 10% of the corresponding rate of spread values. In subsequent plots, we
 308 will omit the uncertainty lines.

309 The fires both achieved approximately the same quasi-equilibrium rate of spread, $R_{qe} \approx$
 310 1.1 m s^{-1} , at approximately 60 s and 50 s after ignition for the inward and outward
 311 protocols, respectively. For both cases this corresponds to 50 m downstream of the ignition
 312 line. The R for the inward ignition protocol fluctuated greatly: between 25 s and 60 s (or
 313 0 to 50 m), with R peaking at approximately 1.7 m s^{-1} . The peak in R has been discussed
 314 by Viegas *et al.* (2012) for merging junction fires. In essence, the inward protocol is similar
 315 to two straight-line fires merging at a V-shaped junction. The acceleration phase should
 316 be enhanced as the ignition line speed decreases, and the fire front closer approximates a
 317 V-shaped junction fire. In contrast, R for the the outward ignition protocol grew steadily
 318 to the quasi-equilibrium value R_{qe} . The initially high rate of spread in the inward ignition
 319 case lead to an overall faster moving fire: the inward ignition protocol reached the end of
 320 the plot a approximately 80 s after ignition and the outwards ignition protocol reached
 the end of the plot at approximately 110 s after ignition.

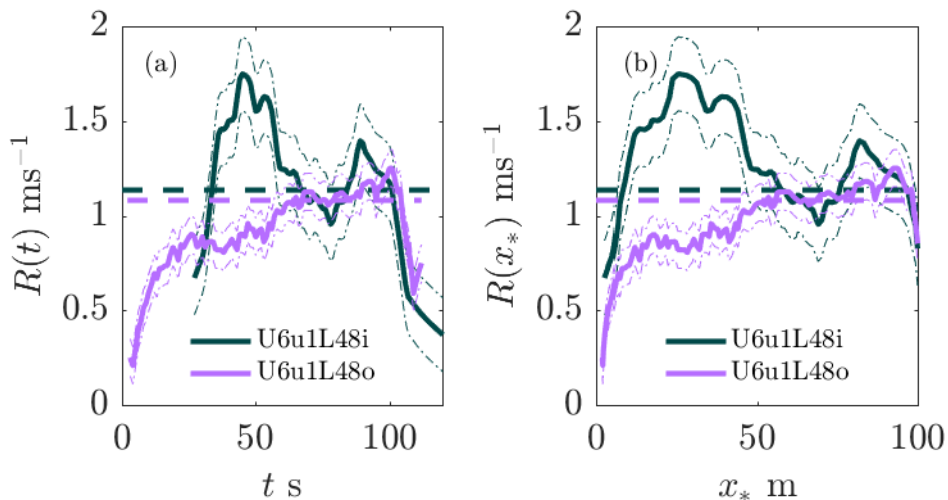


Figure 5: Variation in R for U6u1L48i and U6u1L48o. (a) R is plotted versus time, (b) R is plotted versus fire front location x_* . The thin broken lines are the uncertainties in R estimated from the variance of the data. The thick dashed lines are computed from a linear regression fit to the fire front location x_* in the quasi-equilibrium region.

321

322 The rate of spread as wind speed was varied is shown in Figure 6. The result for the inward

323 ignition protocol for $U_2 = 10 \text{ m s}^{-1}$ was similar to the $U_2 = 6 \text{ m s}^{-1}$ case. Rate of spread
 324 increased for $x_* < 30 \text{ m}$ and then decreased to a quasi-equilibrium value of $R_{qe} \approx 1.5$
 325 m s^{-1} at approximately $x_* = 60 \text{ m}$. However, R for the $U = 3 \text{ m s}^{-1}$ (inward ignition)
 326 case quickly rose to the quasi-equilibrium value at $R_{qe} = 0.9 \text{ m s}^{-1}$. The outwards ignition
 cases all rose steadily to the quasi-equilibrium values.

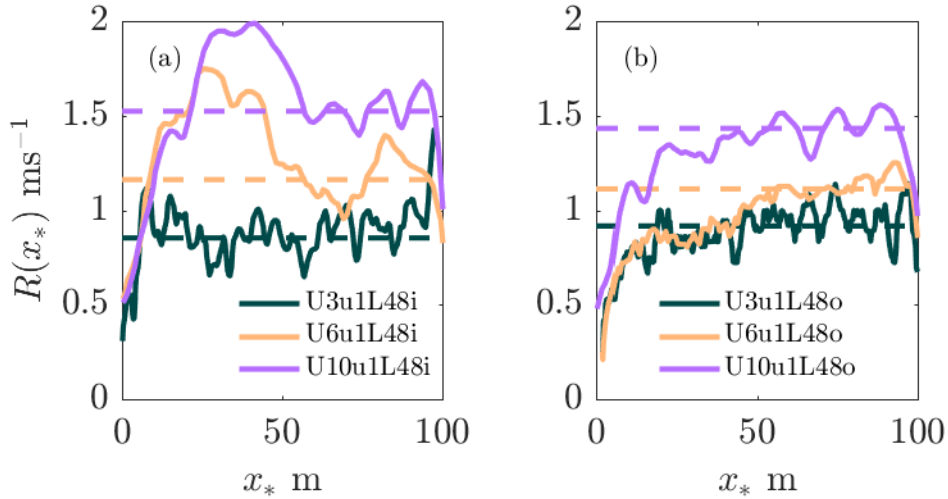


Figure 6: Effect of inlet 2 m wind speed upon R for inward ignition (a) and outward
 ignition (b). The quasi-equilibrium R_{qe} increases with wind speed. The surge behaviour
 is visible in the U10u1L48i case but not the U3u1L48i case nor any of the outward-ignition
 cases.

327

328 The effect of ignition line length upon R is shown in Figure 7. The U6u1L96i case was
 329 aberrant: no quasi-equilibrium was reached and the fire exhibits an acceleration and
 330 deceleration phase like a merging junction fire (Raposo *et al.*, 2018), rather than the
 331 development to a quasi-equilibrium R like the line fires of Cheney *et al.* (1993) and Cruz
 332 *et al.* (2015b). If the U6u1L96i case is considered in isolation, the central part ($40 < x < 60$
 333 m) may be thought to be at a quasi-equilibrium R , especially on a relatively short burn
 334 plot. The trend for the shorter ignition length cases, however, suggests this is a transient
 335 peak in R , and that U6u1L96i does not achieve a quasi-equilibrium R . For all other
 336 cases, there was a slight increase in quasi-equilibrium R_{qe} as the ignition line increases,
 337 however, this trend was neither large nor significant. For the inward ignition cases (except
 338 U6u1L96i): for the $L_i = 12 \text{ m}$ case $R_{qe} \approx 0.94 \text{ m s}^{-1}$ in the quasi-equilibrium regime; for

339 the $L_i = 48$ m case $R_{qe} \approx 1.16$ m s⁻¹. The uncertainty in R is 0.1 m s⁻¹ so the observed
 340 differences are close to the noise level. It should be noted that the difference in R_{qe} at
 341 different ignition lengths is about 25%. Canfield *et al.* (2014) observed that ignition line
 342 length does effect the overall R_{qe} , however, their study considered ignition line lengths of
 343 up to 400 m. The outward ignition cases also showed an increasing trend with increasing
 344 L_i but the magnitude of the increase was small. The U6u1L96o case exhibited greater
 345 fluctuations than the other cases with a lower ignition line length. However, the R_{qe} for
 346 the U6u1L96o case is only approximately 5% higher than for the U6u1L48o case. Cheney
 347 and Gould (1995) suggested that an ignition line of greater than 100 m length is required
 348 to achieve a fire that reaches the quasi-equilibrium spread regime. With the exception
 349 of the U6u1L96i case, the simulation results suggest that L_i does not greatly effect R_{qe} ,
 350 but L_i does effect the variation in $R(t)$ (or equivalently $R(x_*)$). The U6u1L96i case
 351 suggests that the inwards ignition protocol is unsuitable for experimental fires of this size,
 352 where the experiment aims to study line fires. More research is required to completely
 353 understand how fire development depends on the initial size of the fire.

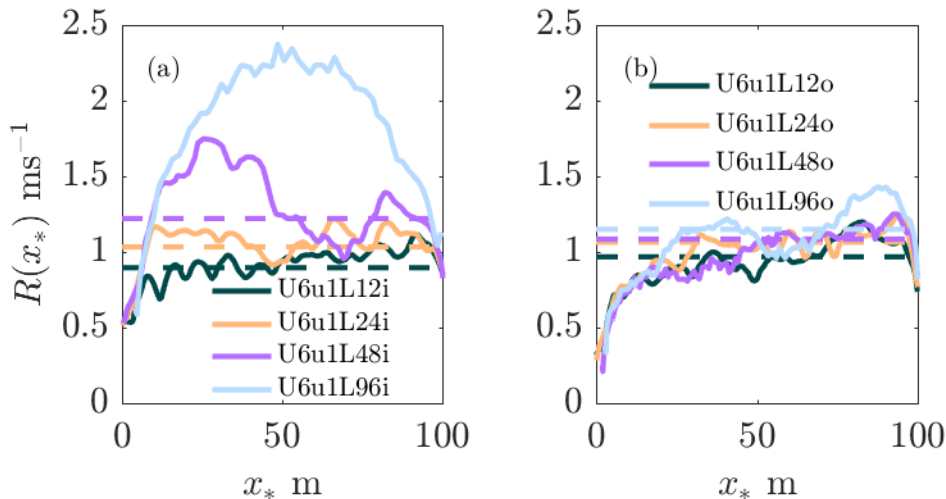


Figure 7: Variation of R with varying ignition line length. The U6u1L96i case is aberrant (see text). For the other cases, some increase in quasi-equilibrium R_{qe} is observed with increasing ignition line length in the inward ignition cases (a), but not with the outwards ignition cases (b).

354 The effect of varying the ignition speed on R is shown in Figure 8. For these simulation
 355 cases, the time taken for the ignition to progress from the starting point to the end point

356 was changed to give the stated ignition speed. Interestingly, the rate of spread of the
 357 outward ignition protocol was not significantly affected by increasing the ignition speed,
 358 however, for the inward ignition R was greatly affected. The faster ignition speed, 2.4
 359 m s^{-1} , achieved a quasi-equilibrium within approximately 20 m. The slower ignition
 360 speed, 0.5 m s^{-1} did not achieve a quasi-equilibrium rate of spread. Due to the slow
 361 ignition speed, two distinct parabolic shaped fires developed and then merged together as
 362 the ignition reached the middle of the plot. The R_{qe} achieved using the outward ignition
 363 protocol seems largely unaffected by ignition line speed. Figure 7(b) shows that the three
 364 simulations appear to give convergent results for $R(x_*)$. Perhaps this is because the head
 365 fire is established immediately at ignition and the head fire grows slowly as the flanks of
 366 the fire develop with subsequent ignition.

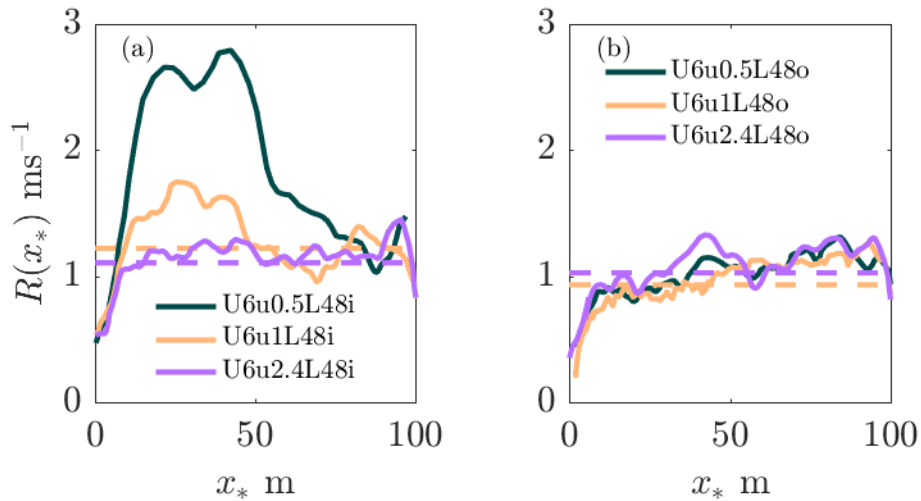


Figure 8: The effect of ignition line speed on R . The inward protocol (a) showed that a faster ignition line speed yields quasi-equilibrium R_{qe} quickly, whereas a slow ignition line speed led to a large surge in R and no overall quasi-equilibrium state. The outwards ignition protocols were unaffected by ignition line speeds (b).

367 Figure 9 compares the U6u1L48i and U6u1L48o cases to an infinite ignition speed simu-
 368 lation (U6uInfL48), in which all 48 m of the initial fire line was ignited simultaneously.
 369 The U6uInfL48 case can be seen as an ignition protocol control simulation representing
 370 the limiting cases of both ignition protocols. This could possibly be realised in experi-
 371 ments by a line of accelerant ignited automatically at many points along the line. The
 372 U6uInfL48 simulation reached a quasi-equilibrium state, at approximately 35 m, which

373 is earlier than the inward and outward protocol simulations for the same wind speed and
374 ignition line length. The U6uInfL48 case also did not exhibit the initial surge observed
375 in the U6u1L48i case.

376 Interestingly, between about $x_* = 10$ m and $x_* = 30$ m, the U6uInfL48 case exhibited a
377 quasi-steady rate of spread that was slightly-lower than the value of R_{qe} attained in the
378 later stages of development.

379 The difference between the smoothed R and the quasi-equilibrium R_{qe} was within the
380 uncertainty level in R (approximately 10%), as measured by the variance of R over the
381 whole simulation time. Overall, faster ignition speed gives an initial fire line which is
382 closer to a straight line and the overall development is more uniform relative to both the
383 inward and outwards ignition protocol cases.

384 In this investigation of the effects of ignition line length and ignition line speed, full
385 factorial experimental design was not considered. Instead the ignition speed was fixed at
386 a single value 1 ms^{-1} and L_i varied; or L_i was fixed at 48 m and u_i was varied. This choice
387 reflects the contemporary experimental protocols used in Cheney *et al.* (1993), Cheney
388 *et al.* (1998), and Cruz *et al.* (2015b). If L_i varies with constant u_i then the time for the
389 ignition to be completed varies and could impact $R(t)$. Because we seek to assess realistic
390 experimental protocols, our choice of varying L_i for a single fixed u_i (and vice versa) will
391 not affect our conclusions. It may be of interest to investigate the effect of ignition time
392 on $R(t)$ in a future study.

393 **Two-dimensional rate of spread development**

394 The normal velocity of the two-dimensional front was obtained through a curve-fitting
395 and extrapolation algorithm. Once the fire established itself as a single continuous fire
396 line, the centre of the pyrolysis region was obtained for each y -point and each time step;
397 that is, $x_*(y_j, t_n)$. A sixth-order polynomial, $p_n(y)$, was fitted to the $x_*(y_j, t_n)$ points.
398 This process was repeated until the fire impinges upon the end of the burning plot. The

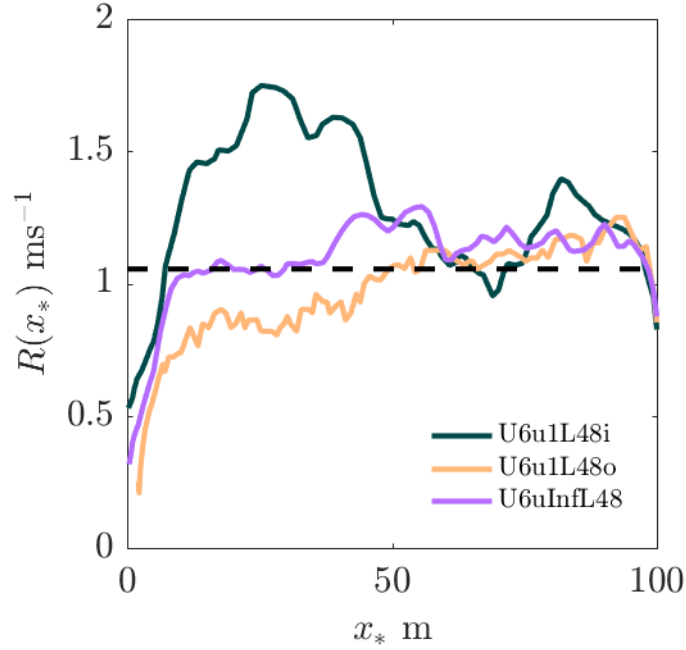


Figure 9: Comparison of the R for U6u1L48i, U6u1L48o, and U6uInfL48, the infinitely fast ignition line simulation.

399 goodness of the polynomial fit is assessed by Pearson's r^2 value; r^2 is always greater
 400 than 0.9 indicating that the sixth-order polynomial fit is adequate. The next part of the
 401 algorithm estimates the normal velocity of the curve by measuring the distance between
 402 $p_n(y_j)$ and $p_{n+1}(y)$ along the line normal to $p_n(y_j)$. Because the time between outputs
 403 $\delta t = t_{n+1} - t_n$ is known, the normal velocity of the curve $p_n(y)$ can be approximated.
 404 For every y_j we compute the line normal to $p_n(y)$ at y_j ; the line is denoted $l_{j,n}(y)$. The
 405 equation of the line is

$$l_{j,n}(y) = p_n(y_j) - \left(\frac{dp_n}{dy}(y_j) \right)^{-1} (y - y_j). \quad (3)$$

406 The point of intersection, y_* , between the $l_{j,n}(y)$ is found by solving

$$p_{n+1}(y_*) - l_{j,n}(y_*) = 0, \quad (4)$$

407 numerically using the Newton-Raphson scheme. The normal velocity at y_j is then

$$u_n(y_j) = \frac{((l_{j,n}(y_*) - p_n(y_j))^2 + (y_* - y_j)^2)^{1/2}}{\delta t}. \quad (5)$$

408 The resulting normal velocity is visualised as a function of y and t . The shaded surfaces
 409 of u_n for U6u1L48i and U6u1L48o are shown in Figure 10. There is minor noise in these
 410 plots, however, additional smoothing as was used. The polynomial fit to the centre of the
 411 pyrolysis region tends to much of the noise in the u_n data.

412 In Figure 10 the inward ignition protocol starts later than the outward ignition protocol;
 413 this is because u_n was computed from the instant a single connected fire line exists. As
 414 shown in Figure 2 the inward ignition protocol was overall much faster to burn to the end
 415 of the plot. To remove difficulties with fitting the polynomial to disconnected regions, the
 416 u_n calculation is stopped before the fires reach the end of the burnable plot.

417 The colouring in Figure 10 separates head fire motion (fast, yellow) from flank fire motion
 418 (slow, blue). The figure illustrates the growth in overall fire line width, which occurs in
 419 two phases. At approximately 50 s the fire line increased in width, however, the edges
 420 have low u_n -velocity so this increase corresponded to a thickening of the flanks of the
 421 fire. Some increase in the head fire width was apparent but this was minor; for both
 422 cases the head fire appears fairly well constrained to the range $-20 < y < 20$ m. The
 423 emergence of the quasi-equilibrium state is also apparent in these surface plots.

424 The speed u_n appeared to equilibrate after approximately 70 s for both the inward ignition
 425 protocol and outwards ignition protocol. For the outwards ignition protocol, however,
 426 more simulation time is required to make this conclusion definitive. The most prominent
 427 feature was the large local maximum of u_n for the inward ignition case. This maximum
 428 shows the centre of the fire rushing forwards from approximately $t = 40$ s to $t = 60$
 429 s. This is consistent with the centreline velocity shown in Figure 5(a). Comparing the
 430 spatial velocity pattern in Figure 10(b) with the development of the fire depicted in Figure
 431 2(b) reveals that the region of maximum u_n corresponds to the stage of fire development
 432 in which the fireline exhibited a region of negative curvature. The increased velocity is
 433 localised to the region of negatively curved fire line, which accelerated forward. The rate

434 of spread decreased back to the quasi-equilibrium R_{qe} once the fireline had achieved its
 435 final, roughly parabolic, shape. This localised increase in the rate of spread is consistent
 436 with the observations of Hilton *et al.* (2017) and Hilton *et al.* (2018). Hilton *et al.* (2018)
 437 demonstrated that the acceleration in the fireline is a convective effect. The fire produces
 438 a buoyancy-driven flow which is enhanced in regions of negative curvature, in turn leading
 439 to acceleration of the fire.

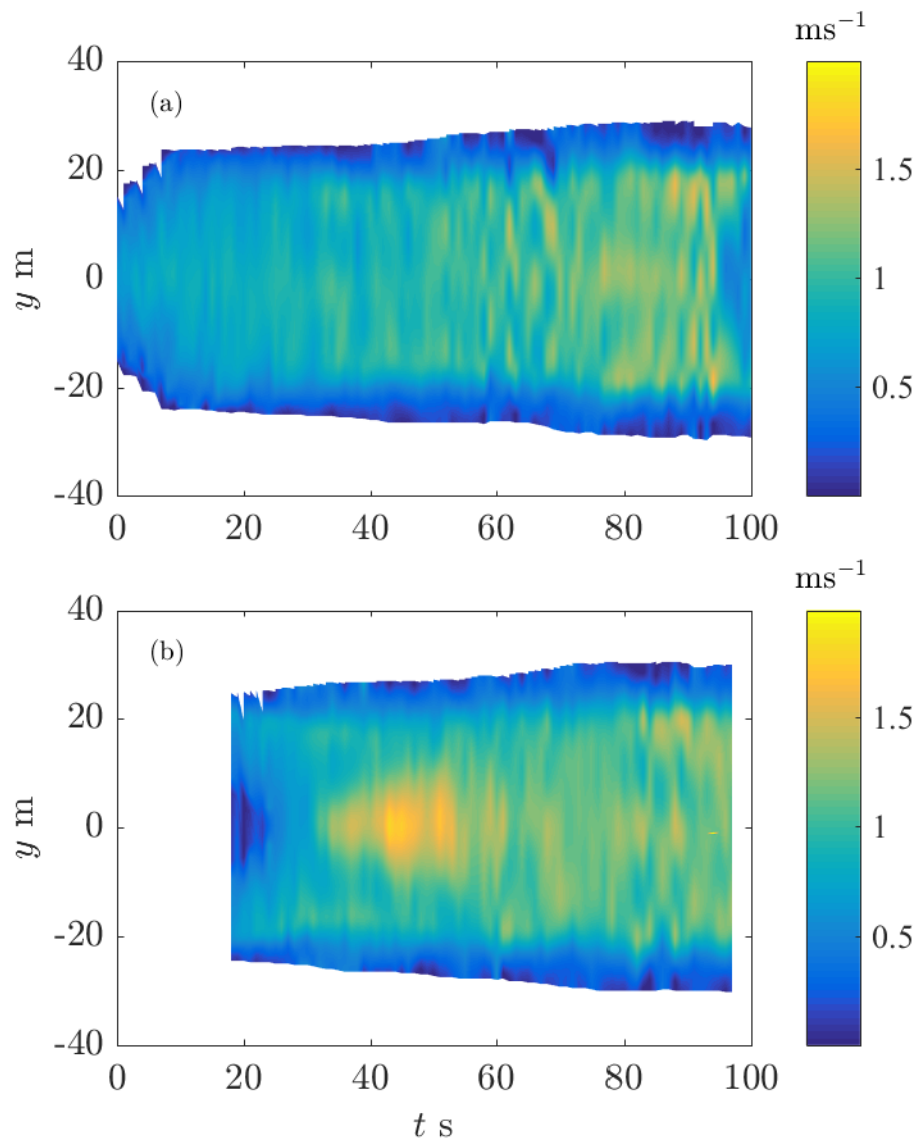


Figure 10: The speed of the fire front as a function of time and y-distance. (a) Outwards ignition (b) inward ignition.

Convective number development

Recently, Morvan and Frangieh (2018) attempted to clarify the use of dimensionless parameters to characterise fire behaviour as wind-driven or buoyancy-driven fires.

Morvan and Frangieh (2018) characterised fires using the Byram number:

$$N_c = \frac{2gQ}{(U_{10} - R)^3 \rho c_p T_a}. \quad (6)$$

Here U_{10} is a velocity scale far from the flame, taken here as the time averaged velocity at the fire ground at 10 m, i.e. $\bar{u}(405, 50, 10)$. The unitless factor of two acts only as a scaling and contributes no information; we retain it only for consistency with the literature. The other parameters used to compute N_c were the ambient temperature in the simulation $T_a = 305$ K, the density $\rho = 1.2$ kg m⁻³ and specific heat of air $c_p = 1.0$ kJ kg⁻¹ K⁻¹.

Morvan and Frangieh (2018) provided bounds on N_c to classify a fire as wind-driven or buoyancy-driven. Using data from wildfires and experimental fires Morvan and Frangieh determined that if $N_c > 10$ the fire is buoyancy-driven, and if $N_c < 2$ the fire is wind-driven – this is consistent with $\mathcal{O}(N_c) = 1$ for transition between the two modes. At intermediate N_c values the fire is neither buoyancy-driven nor wind-driven. It is hypothesised that an intermediate regime, called the surge-stall regime Dold and Zinoviev (2009); Dold (2010), occurs in the intermediate range of N_c where the fire oscillates between the wind-driven and buoyancy-driven modes.

Intensity at each time step Q_n was computed as the globally averaged heat release rate, divided by the fire line length measured along the centre of the pyrolysis region at each time step. The fire line length was determined using the arc length of the polynomial fit, $p_n(y)$, to the centre of the pyrolysis region. That is

$$Q = \frac{\langle HRR \rangle}{\int_{y_i}^{y_f} \left(1 + \left(\frac{dp_n}{dy} \right)^2 \right)^{1/2} dy}. \quad (7)$$

461 Note that the integral was computed from the first burning y -location, y_i to the final
462 burning y -location, y_f . Using mid-flame measurements of wind as the relevant velocity
463 scale could be more appropriate; however it seems that the choice of best wind scale in
464 the Byram number is still an open problem. Using mid-flame measurements would change
465 the N_c values computed here.

466 The simulated N_c for all cases is shown in Figure 11. There is an increase in N_c for $x_* < 50$
467 m for the inward ignition cases (shown in Figure 11(a) and Figure 11(c)), however with
468 the exception of the U6u0.5L48i and U6Lu1L96i cases, the fires are still within the wind
469 driven regime. The N_c for the U6u0.5L48i and U6Lu1L96i cases indicates that the initial
470 surge of these fires are transitional and possibly within the so-called surge-stall regime
471 (Dold and Zinoviev, 2009; Dold, 2010). Greater insight into fires with $2 < N_c < 10$ is
472 required to understand and completely classify fires in the surge-stall regime.

473 The two lowest wind speed cases (shown in Figure 11(b)) are classified as buoyancy
474 dominated given the large N_c . Note the large value of N_c is consistent with observations
475 for grass fires of Morvan and Frangieh (2018).

476 The application of dimensional analysis to characterise fire behaviour simulated here
477 would also be of interest. Provided that dimensionless parameters are used, the resulting
478 characterisation of fires should be equivalent, regardless of the individual scales chosen.
479 Such analysis would allow more general models of fire spread to be constructed, however,
480 such a study is beyond the scope of the present work.

481 Conclusions

482 The simulation results demonstrate that the ignition protocol effects the development
483 of a fire to its quasi-equilibrium rate of spread. The ignition protocol may then effect
484 statistical analysis of experimental results, however, it is not known which, if any, historic
485 experimental results will be adversely affected. It is possible that, particularly for inward
486 ignition cases with a large initial acceleration of the fire, experimental fires could have

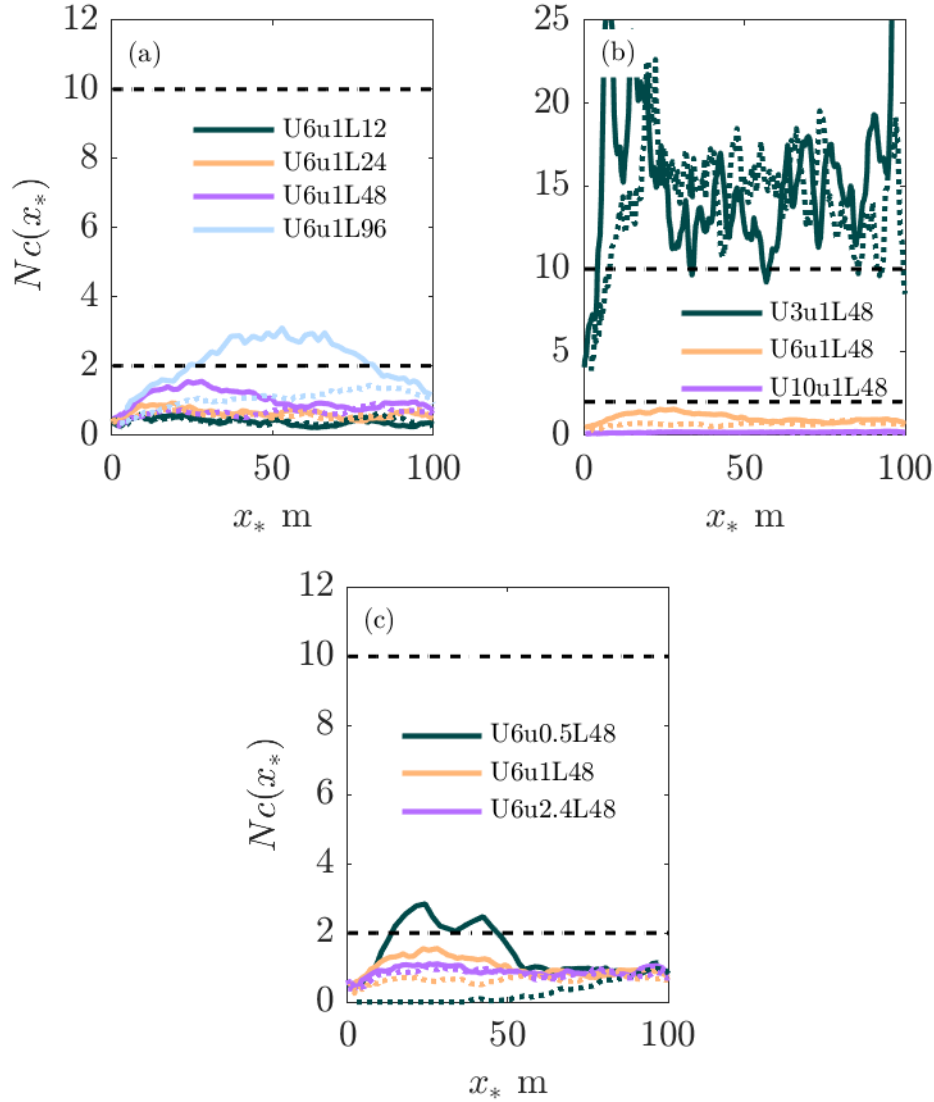


Figure 11: Byram numbers for all cases. (a) Variation in ignition line length, (b) variation of wind speed (c) variation in ignition speed. The solid line represents the inward ignition protocol and the dashed line is the outward protocol.

487 been measured in a surge-stall regime which may led to overestimated R_{qe} . The
 488 simulated fires typically develop to a quasi-equilibrium rate of spread in approximately
 489 50 m (over a 100 m) plot, consistent with Cruz *et al.* (2015b) who observed that the
 490 fire took approximately half of the plot length to develop to a quasi-equilibrium spread
 491 rate. However, Cruz *et al.* (2015b) made this observation on much smaller burn plots (33
 492 m on each side). We observed that the ignition line length in the inward ignition cases
 493 appeared to influence the development to a quasi-equilibrium R_{qe} , however, we did not
 494 test the effect of a narrower burnable plot.

495 Experimental fires are often complicated by variable wind fields, non-homogeneous fuels,
496 and rough terrain. Therefore, researchers must be cautious when using the results of sim-
497 ulation studies to inform experimental practice. However, the simulated inward ignition
498 protocol $R(x_*)$ results are overwhelming: using the inward ignition protocol with a mod-
499 est to slow ignition line speed in typical wind conditions yields a fire that surges forward
500 rather than developing monotonically to a quasi-equilibrium rate of spread. Experimen-
501 talists should seek to establish a quasi-equilibrium rate of spread as quickly as possible
502 and ensure that experimental plots are of sufficient length so that (a) the fire does indeed
503 achieve a quasi-equilibrium state, and (b) the fire does not undergo unintended surging
504 behaviour, or the surging behaviour has subsided before data is sampled. Therefore, the
505 simulation results suggest that the inward ignition protocol should not be used. The out-
506 ward ignition protocol does not produce oscillations and overall may be a more prudent
507 choice. If available, an automatic ignition line that gives an effectively infinite ignition
508 line speed appears preferable.

509 Given the emergence of drone technology and high speed videography, it is possible to
510 accurately record the position of an experimental fire at high temporal resolution. Sulli-
511 van *et al.* (2018) have studied the development of fires from a point ignition using drone
512 footage and were able to measure the development in the rate of spread. Measuring R
513 as a function of time (or distance) is a valuable experimental endeavour. Such informa-
514 tion would facilitate additional validation for physics-based simulations, but would also
515 support refined statistical analyses of the experimental results. Collecting such detailed
516 information over a range of wind speeds, and complementing experimental analyses with
517 further numerical simulations, could also provide additional insights into the surge-stall
518 regime.

519 **Acknowledgements**

520 This research was supported by the Bushfire and Natural Hazards Cooperative Research
521 Centre and some computational resources were provided by the University of Melbourne

522 Research Platforms. This research was also undertaken with the assistance of resources
523 and services from the National Computational Infrastructure (NCI), which is supported
524 by the Australian Government.

525 **Conflicts of Interest**

526 The authors declare no conflicts of interest.

Nomenclature

t	s	time
x, y	m	streamwise and lateral coordinates, respectively
t_n	s	the time at the n^{th} time step
y_j	m	the j^{th} grid point in the y -direction
y_i, y_f	m	minimum and maximum y -locations that are burning at a particular time step
U_2	m s^{-1}	the inlet wind speed, specified at 2 m above the ground
U_{10}	m s^{-1}	velocity scale for the Byram number; taken as the u -velocity at 10 m from the ground over the burnable plot
u, v, w	m s^{-1}	fluid velocities, a prime ($'$) denotes the fluctuation from the mean
L_i	m	Ignition line length
L_D	m	Domain length
u_i	m	Ignition line speed
l	m	descretised ignition line segment $l = L_i/8$
δt	s	simulation time step
δt_i	s	descretised ignition time step $\delta t_i = l/u_i$
x_0 and x_1	m	trailing and leading edges of the pyrolysis region along $y = 0$ respectively.
x_*	m	fire location on the centreline. The mid-point between x_0 and x_1 , strictly a function of time.
$x * (y_j, t_n)$	m	fire location in the lateral grid point y_j , at time step t_n .
R	m s^{-1}	Rate of spread
$R(t) R(x_*)$	m s^{-1}	R as a function of time or distance from the ignition
R_{qe}	m s^{-1}	Quasi-equilibrium rate of spread
τ	s	domain turnover timescale, i.e. the length of the domain divided by a characteristic velocity
r^2		goodness of fit statistic.
$p_n(y)$		a 6^{th} order polynomial fitted to the fire line at time step t_n
$l_{j,n}(y)$		a line starting at y_j at time step t_n used in the calculation of the normal velocity of the fire line
y_*	m	point of intersection between the construction line $l_{j,n}(y)$ and the fire line $p_{n+1}(y)$ at the subsequent time step
$u_n(y_j)$	m s^{-1}	the normal velocity of the fire line at lateral location y_j and time step t_n
u_n	m s^{-1}	the normal velocity of the fire line, a function of time and y -location
N_c		Byram number
$T_a = 305$	K	ambient temperature
$\rho = 1.2$	kg m^{-3}	density of air
$c_p = 1.0$	$\text{kJ kg}^{-1} \text{K}^{-1}$	specific heat of air .
$g = 9.8$	m s^{-2}	gravitational acceleration
Q	kW m^{-1}	fire intensity.
HRR	kW	Heat release rate

References

- 528
- 529 Apte, VB, Bilger, RW, Green, AR, and Quintiere, JG (1991) Wind-aided turbulent flame
530 spread and burning over large-scale horizontal PMMA surfaces. *Combustion and Flame*
531 **85**, 169–184. doi:10.1016/0010-2180(91)90185-E.
- 532 Belcher, SE, Harman, IN, and Finnigan, JJ (2012) The wind in the willows: flows in
533 forest canopies in complex terrain. *Annual Review of Fluid Mechanics* **44**, 479–504.
534 doi:10.1146/annurev-fluid-120710-101036.
- 535 Bou-Zeid, E, Meneveau, C, and Parlange, MB (2004) Large-eddy simulation of neutral
536 atmospheric boundary layer flow over heterogeneous surfaces: Blending height and ef-
537 fective surface roughness. *Water Resources Research* **40**. doi:10.1029/2003WR002475.
- 538 Canfield, JM, Linn, RR, Sauer, JA, Finney, M, and Forthofer, J (2014) A numerical
539 investigation of the interplay between fireline length, geometry, and rate of spread.
540 *Agricultural and Forest Meteorology* **189**, 48–59. doi:10.1016/j.agrformet.2014.
541 01.007.
- 542 Cheney, NP and Gould, JS (1995) Fire growth in grassland fuels. *International Journal*
543 *of Wildland Fire* **5**, 237–247. 10.1071/WF9950237.
- 544 Cheney, NP, Gould, JS, and Catchpole, WR (1993) The influence of fuel, weather and fire
545 shape variables on fire-spread in grasslands. *International Journal of Wildland Fire* **3**,
546 31–44. doi:10.1071/WF9930031.
- 547 Cheney, NP, Gould, JS, and Catchpole, WR (1998) Prediction of fire spread in grasslands.
548 *International Journal of Wildland Fire* **8**, 1–13. doi:10.1071/WF9980001.
- 549 Cruz, MG, Gould, JS, Alexander, ME, Sullivan, AL, McCaw, WL, and Matthews, S
550 (2015a) A guide to rate of fire spread models for Australian vegetation. Australasian
551 Fire and Emergency Service Authorities Council Limited and Commonwealth Scientific
552 and Industrial Research Organisation.

- 553 Cruz, MG, Gould, JS, Kidnie, S, Bessell, R, Nichols, D, and Slijepcevic, A (2015b) Ef-
554 fects of curing on grassfires: II. effect of grass senescence on the rate of fire spread.
555 *International Journal of Wildland Fire* **24**, 838–848. doi:10.1071/WF14146.
- 556 Dold, JW (2010) Vegetation engagement in unsteady fire spread. In ‘Proceedings of the
557 VI International Conference on Forest Fire Research’, pages 15–18.
- 558 Dold, JW and Zinoviev, A (2009) Fire eruption through intensity and spread rate inter-
559 action mediated by flow attachment. *Combustion Theory and Modelling* **13**, 763–793.
560 doi:10.1080/13647830902977570.
- 561 Forney, GP (2019) Smokeview, A Tool for Visualizing Fire Dynamics Simulation Data
562 Volume I: Users Guide. US Department of Commerce, National Institute of Standards
563 and Technology.
- 564 Frangieh, N, Morvan, D, Meradji, S, Accary, G, and Bessonov, O (2018) Numerical sim-
565 ulation of grassland fires behavior using an implicit physical multiphase model. *Fire*
566 *Safety Journal* **102**, 37–47. doi:10.1016/j.firesaf.2018.06.004.
- 567 Hilton, JE, Miller, C, Sharples, JJ, and Sullivan, AL (2017) Curvature effects in the
568 dynamic propagation of wildfires. *International Journal of Wildland Fire* **25**, 1238–
569 1251. doi:10.1071/WF16070.
- 570 Hilton, JE, Sullivan, AL, Swedosh, W, Sharples, J, and Thomas, C (2018) Incorporating
571 convective feedback in wildfire simulations using pyrogenic potential. *Environmental*
572 *Modelling & Software* **107**, 12–24. doi:10.1016/j.envsoft.2018.05.009.
- 573 Linn, RR and Cunningham, P (2005) Numerical simulations of grass fires using a coupled
574 atmosphere–fire model: basic fire behavior and dependence on wind speed. *Journal of*
575 *Geophysical Research: Atmospheres* **110**, D13107. doi:10.1029/2004JD005597.
- 576 McDermott, R, McGrattan, KB, and Floyd, J (2011) A simple reaction time scale for
577 under-resolved fire dynamics. *Fire Safety Science* **10**, 809–820. doi:10.3801/IAFSS.
578 FSS.10–809.

579 McGrattan, K, Hostikka, S, Floyd, J, Jand Baum, HR, Rehm, RG, Mell, W, and McDer-
580 mott, R (2013) Fire dynamics simulator (version 6), technical reference guide. *NIST*
581 *special publication* **1018**.

582 Mell, W, Jenkins, MA, Gould, J, and Cheney, P (2007) A physics-based approach to
583 modelling grassland fires. *International Journal of Wildland Fire* **16**, 1–22. doi:
584 10.1071/WF06002.

585 Moinuddin, KAM, Sutherland, D, and Mell, W (2018) Simulation study of grass fire
586 using a physics-based model: striving towards numerical rigour and the effect of grass
587 height on the rate-of-spread. *International Journal of Wildland Fire* **27**, 800–814.
588 doi:10.1071/WF17126.

589 Morvan, D and Dupuy, JL (2004) Modeling the propagation of a wildfire through a
590 mediterranean shrub using a multiphase formulation. *Combustion and Flame* **138**,
591 199–210. doi:10.1016/j.combustflame.2004.05.001.

592 Morvan, D and Frangieh, N (2018) Wildland fires behaviour: wind effect versus byrams
593 convective number and consequences upon the regime of propagation. *International*
594 *Journal of Wildland Fire* **27**, 636–641. doi:10.1071/WF18014.

595 Morvan, D, Meradji, S, and Mell, W (2013) Interaction between head fire and backfire in
596 grasslands. *Fire Safety Journal* **58**, 195–203. doi:10.1016/j.firesaf.2013.01.027.

597 Raposo, JR, Viegas, DX, Xie, X, Almeida, M, Figueiredo, AR, Porto, L, and Sharples, J
598 (2018) Analysis of the physical processes associated with junction fires at laboratory and
599 field scales. *International Journal of Wildland Fire* **27**, 52–68. doi:10.1071/WF16173.

600 Sullivan, AL, Cruz, MG, Hilton, JE, Plucinski, MP, and R., Hurley (2018) Study of growth
601 of free-burning grass fires from point ignition. In ‘Proceedings of the VIII International
602 Conference on Forest Fire Research’, pages 643–649.

603 Viegas, DX, Raposo, JR, Davim, DA, and Rossa, CG (2012) Study of the jump fire
604 produced by the interaction of two oblique fire fronts. part 1. analytical model and

605 validation with no-slope laboratory experiments. *International Journal of Wildland*
606 *Fire* **21**, 843–856. doi:10.1071/WF10155.